CONDENSED MATTER PHYSICS

Reappearance of first Shapiro step in narrow topological Josephson junctions

Daniel Rosenbach[1,2,3]*†‡, Tobias W. Schmitt[1,4†], Peter Schüffelgen[1,2], Martin P. Stehno[5], Chuan Li[6], Michael Schleenvoigt[1], Abdur R. Jalil[1], Gregor Mussler[1,2], Elmar Neumann[7], Stefan Trellenkamp[7], Alexander A. Golubov[6§], Alexander Brinkman[6], Detlev Grützmacher[1,2], Thomas Schäpers[1,2,3]

In Josephson junctions, a supercurrent across a nonsuperconducting weak link is carried by electron-hole bound states. Because of the helical spin texture of nondegenerate topological surface states, gapless bound states are established in junctions with topological weak link. These have a characteristic 4π-periodic current phase relation (CΦR) that leads to twice the conventional Shapiro step separation voltage in radio frequency–dependent measurements. In this context, we identify an attenuated first Shapiro step in $(Bi_{0.06}Sb_{0.94})_2Te_3$ (BST) Josephson junctions with AlO_x capping layer. We further investigate junctions on narrow, selectively deposited BST nanoribbons, where surface charges are confined to the perimeter of the nanoribbon. Within these junctions, previously identified signatures of gapless bound states are absent. Because of confinement, transverse momentum sub-bands are quantized and a topological gap opening is observed. Surface states within these quantized sub-bands are spin degenerate, which evokes bound states of conventional 2π-periodic CΦR within the BST nanoribbon weak link.

INTRODUCTION

Superconducting topological hybrid devices consist of topological matter that is partially covered with metallic, s-wave superconductors. These devices are frequently studied for their implementation in complex topological quantum computation schemes (*1*–*3*) that are based on the local arrangement of Majorana zero modes (*4*–*5*). These exotic quasi-particles arise at the interface of topological matter with helical, spin nondegenerate surface states (*6*, *7*) toward a superconducting metal, as the proximity coupling gives rise to unconventional pairing mechanisms (*5*).

In topological Josephson junctions, two closely spaced superconducting electrodes are defined on top of a topological weak link. Owing to the proximity effect, superconducting properties are induced into the topological matter right underneath the superconducting electrodes. In between these two proximity coupled regions, a Josephson supercurrent of *2e* charge is carried by electron-hole bound states. The unique helical spin texture within the topological weak link evokes gapless Majorana bound states (MBSs) (*5*, *8*–*10*). The current phase relation (CΦR) of these MBSs has a doubled periodicity when compared to conventional Andreev bound states (ABSs) (*11*). The unconventional CΦR can be probed in either superconducting quantum interference devices (*12*), phase-controlled Josephson junctions (*13*), or biased Josephson junctions by performing Shapiro step measurements (*8*, *14*–*17*). Signatures of MBSs in Shapiro step measurements have already been reported in three-dimensional (3D) topological insulators (TIs) (*8*, *17*, *18*), topological semimetals (*16*), and 2D TIs (*15*).

On the verge in between basic material research and technological implementation, novel fabrication techniques are used to pursue a high device quality with high yield (*17*, *19*). One main aspect for superconducting topological hybrid devices is to ensure a highly transparent interface between the topological matter and the superconducting metal deposited. Complex in situ deposition techniques have been developed in these regards, which have been reported to lead to contaminant-free interfaces, high transparencies, and a strong proximity coupling (*17*, *19*). We recently reported on molecular beam epitaxy (MBE)–grown, in situ defined TI Josephson junctions on ternary compound $(Bi_{0.06}Sb_{0.94})_2Te_3$ (BST) thin films (*17*). Next to ensuing a high-quality interface, a dielectric capping layer is applied in situ, which keeps the TI pristine. Applying these in situ fabrication techniques leads to measurably high transparencies and the revelation of unconventional 4π-periodic CΦRs by identifying a missing first Shapiro step in as-defined BST Josephson junctions.

In situ preparation techniques often require complex layouts, multiple intra-dependent processing steps, and a high standard of available ultrahigh vacuum clusters. While it is undeniable that this effort is necessary for large-scale production of devices, it can slow down basic material research of previously unindentified topological compounds. Furthermore, conventional lift-off processes allow a more flexible device layout without the need to get rid of any excess superconducting metal. In this article, we evaluate the performance of standard ex situ defined Josephson junctions with respect to observing signatures of MBSs in radio frequency (rf) measurements. Although the interface transparency and thereby the maximum amount of Josephson supercurrent carried by the junction are expected to reduce, the formation of bound states in the topological weak link will sustain, once a proximity gap is induced. After the superconducting electrodes are deposited using conventional ex situ preparation techniques, the topological thin films are capped

[1]Peter Grünberg Institute (PGI-9), Forschungszentrum Jülich, 52425 Jülich, Germany. [2]Helmholtz Virtual Institute for Topological Insulators (VITI), Forschungszentrum Jülich, 52425 Jülich, Germany. [3]JARA-Fundamentals of Future Information Technology, Jülich-Aachen Research Alliance, Forschungszentrum Jülich and RWTH Aachen University, Aachen, Germany. [4]JARA-FIT Institute Green IT, RWTH Aachen University, 52062 Aachen, Germany. [5]Physikalisches Institut EP3, University of Würzburg, Am Hubland 97070, Würzburg, Germany. [6]MESA+ Institute for Nanotechnology, University of Twente, 7500AE Enschede, The Netherlands. [7]Helmholtz Nano Facility (HNF), Forschungszentrum Jülich, 52425 Jülich, Germany.
*Corresponding author. Email: d.rosenbach@utwente.nl
†These authors contributed equally to this work.
‡Present address: MESA+ Institute for Nanotechnology, University of Twente, 7500AE Enschede, The Netherlands.
§Present address: Moscow Institute of Physics and Technology, Dolgoprudny, Moscow Region 14170, Russia.

using an AlO_x capping layer. The capping is applied by depositing a thin layer of aluminum in situ, that oxidizes ex situ, which has previously been reported to successfully keep the TI surface pristine (*20*). The linear surface bands of TIs have been reported to vanish without effective protection (*21*). In uncapped junctions, signatures of 4π-periodic supercurrents are generally not observed (*22*).

In addition, we explore the behavior of junctions with reduced width of the BST weak link. TI nanoribbons that are only 200 nm wide are deposited using a selective area growth (SAG) approach (*23*, *24*). In nanoribbon geometries, transverse momentum states are quantized due to the confinement of surface charges on the nanoribbon perimeter *P*. The quantization leads to a bandgap opening within the Dirac surface states, which become spin degenerate (*25*–*28*). A topological phase transition can be observed by applying a magnetic flux of magnitude $\Phi_0/2 = h/2e$ along the nanoribbon axis (*26*, *28*, *29*). Signatures of a periodic gap opening in magnetotransport measurements on synthesized TI nanowires (*30*–*35*) and just recently in MBE selectively grown nanoribbons (*36*, *37*) have been reported. In Josephson junctions based on confined TI nanoribbons, MBSs vanish without applied magnetic flux due to the spin degeneracy of surface states. The Josephson supercurrent is therefore expected to be carried by conventional ABSs with a 2π-periodic CΦR (*27*). Our investigations on the Shapiro response of wide and narrow Josephson junctions, which were capped in situ, but contacted by conventional ex situ techniques, provide evidence for the quantization of topological surface sub-bands in confined topological weak links.

RESULTS

Josephson junctions have been defined on MBE-grown 3D TI ternary compound BST (*38*) weak links, as schematically shown in Fig. 1A. To keep the BST thin film from degrading in air, an AlO_x capping is applied by depositing a thin film (≈2 nm) of aluminum in situ. The thin aluminum layer will fully oxidize when the sample is exposed to air. Nb superconducting electrodes (30 nm thick) are deposited on top of the BST thin film using magnetron sputtering. The contact area is prepared using a combination of a wet chemical treatment to remove the AlO_x capping locally and a soft Ar-plasma etch before Nb deposition (see Materials and Methods for more information). Geometries of investigated lateral topological Josephson junctions are listed in Table 1. Three wide junctions of $W = 600$ nm on thin films of the BST ternary TI and two narrow junctions on $W =$ 200-nm-wide, selectively deposited BST nanoribbons have been investigated. Junctions have been characterized performing standard dc + ac biased four-terminal measurements inside a dilution refrigerator with 12-mK base temperature. The measured values for the critical current I_c, the normal state resistance R_N, and, as a figure of merit, the I_cR_N product of the junctions are listed in Table 1.

In lateral direction, the Josephson junction is defined in between the proximitized TI (Fig. 1A, green, characterized by the induced superconducting gap of size Δ*) and the nonproximitized TI (light green/olive). Within the nonproximitized region, a supercurrent flows, based on coherent Andreev and reverse Andreev reflection processes that form electron-hole bound states, as depicted in Fig. 1B (dotted line). An electron incident at the TI/S interface might be reflected as an electron or Andreev reflected as a hole. In case of Andreev reflection, a charge of 2*e* is successfully transmitted into S. In case of normal reflection, no charge will be transmitted. The spin of the incident electron will be flipped, as the spin of charges in the topological surface states is locked to their momentum (*6*, *39*). For perpendicular incident charges, normal reflections at the TI/S interface are prohibited, as these two electronic states in spin nondegenerate topological surface states are orthogonal. These perfectly transmitted MBSs are gapless and characterized by a 4π-periodic CΦR (see Fig. 1C, turquoise) (*10*). For nonperpendicular incident

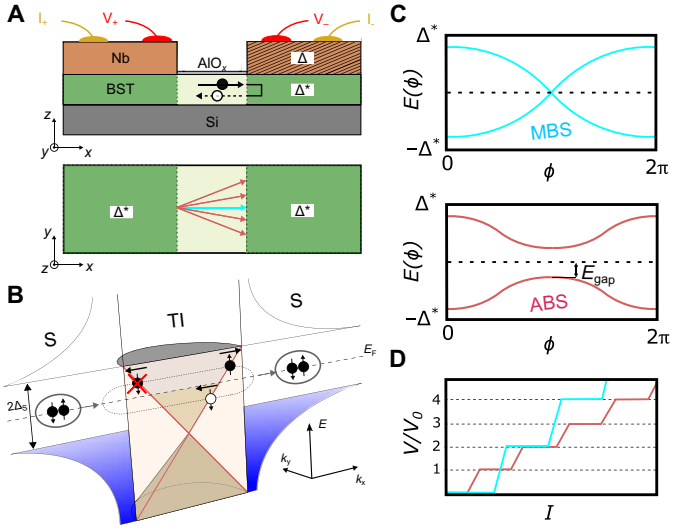

Fig. 1. Schematic representation of the BST thin-film Josephson junctions. (**A**) The Nb electrodes described by the order parameter Δ induce a proximity coupled order parameter of size $\Delta^* \leq \Delta$ within the BST thin film underneath. Within the nonproximitized regions of the BST thin film, a supercurrent will flow, which is carried by MBSs (turquoise) and ABSs (magenta). (**B**) A supercurrent of charge 2*e* is transferred across the TI weak link by coherent electron-hole bound states (dotted line) that are based on the Andreev and reverse Andreev reflection process at the TI/S and S/TI interface, respectively. For perpendicular incident modes [turquoise arrow in (A)], normal reflections at the TI/S interface are suppressed due to orthogonality of both electronic states involved. The resulting bound states are gapless MBSs. For nonperpendicular modes, the probability of normal reflections is nonzero, establishing ABSs with a finite gap E_{gap}. (**C**) The relation of the bound states energy with respect to the superconducting phase difference in between the superconducting electrodes is 2π-periodic for ABSs and 4π-periodic for MBSs. (**D**) In Shapiro step experiments, the ABSs result in integer steps of the Shapiro step separation voltage V_0, while MBSs result in only even integer steps.

Table 1. Overview of Josephson junctions characterized, comparing the critical current I_c, the normal state resistance R_N, and the I_cR_N product for different geometries. Three 600-nm-wide ex situ defined junctions (JJ-wide1 to JJ-wide3) and two narrow Josephson junctions (JJ-narrow1 and JJ-narrow2) on selectively deposited TI nanoribbons have been characterized.

Junction	Width *W* (nm)	Length *L* (nm)	I_c (nA)	R_N (ohms)	I_cR_N (μV)
JJ-wide1	600	130	50	73	3.7
JJ-wide2	600	60	225	68	15.2
JJ-wide3	600	30	400	61	24.4
JJ-narrow1	200	31	30	540	16.2
JJ-narrow2	200	90	24	650	15.6

charges, regular ABSs with a finite gap E_{gap} and a 2π-periodic CΦR are established (see Fig. 1C, magenta) (*40*).

While applying an rf signal, the junctions CΦR can be probed in the bias state by performing Shapiro step measurements (*8*, *9*, *16*). Shapiro steps that are constant potential plateaus in the junction *IV* characteristics appear when an external rf signal is applied to the junction. This induces an additional ac driving current $I_{rf} = I_{ac} \sin(\omega_{ac} t)$ bias, which is superimposed onto the applied dc bias I, where ω_{ac} is the oscillatory frequency and I_{ac} the rf-induced ac amplitude. As the time derivative of the phase difference in between the two superconducting contacts is directly proportional to the voltage across the junction, Shapiro steps show when the rf drive is phase-locked to the junction dynamics (as schematically shown in Fig. 1C). These Shapiro steps are separated by an integer number of a characteristic voltage V_0 that is directly dependent on the periodicity of the bound states CΦR (*14*). Shapiro steps in a system with purely 2π-periodic states (blue curve) appear at every integer of this Shapiro step separation voltage

$$V_0 = \frac{\hbar}{2e}\omega_{ac} \quad (1)$$

where $\hbar$ is the reduced Planck constant. For MBSs, a 4π-periodic CΦR will result in constant potential plateaus of twice the conventional Shapiro step separation voltage V_0.

Figure 2 (A and B) shows the Shapiro response of junction JJ-wide3 at 6.0-GHz and 4.0-GHz excitation frequency, respectively. The differential resistance is shown as a function of the rf power level P and the applied dc bias I. The power level of the applied rf scales with the square of the rf-induced ac amplitude $P \propto |I_{ac}|^2$. When measuring the differential resistance as a function of the dc bias current across a Josephson junction, the constant potential Shapiro steps within the *IV* characteristics will display zero differential resistance ($dV/dI = 0$) areas. To identify the index of observed steps, *IV* curves are shown in Fig. 2C. Here, linecuts are extracted at −10 dBm from the presented data at 4.0 GHz (red curve) and 6.0 GHz (black curve) within Fig. 2 (A and B). The data are presented showing the potential on the ordinate axis, which is divided by the Shapiro step separation voltage V_0. At both excitation frequencies, all integer Shapiro steps are visible. At 4.0 GHz, however, the width of the first integer Shapiro step (in nanoamperes) is reduced, compared to higher integer steps, while in conventional Josephson junctions the first Shapiro step is wider than higher integer steps. At 6.0 GHz, the first integer Shapiro step is wider than the second integer Shapiro step. Comparing the width of the first integer Shapiro step at 4.0 and 6.0 GHz shows that in as-defined junctions, an attenuation of the first step at low frequencies can be observed. This can be observed within the dV/dI measurements (see Fig. 2C), as the total area of the first step at 4 GHz is strongly reduced, compared to higher integer Shapiro steps. An attenuation of the first integer Shapiro step has been observed at intermediate frequencies, before it vanishes completely at even lower frequencies (*8*, *17*). On the basis of this crossover frequency of $f_{4\pi} \leq 4$ GHz, in which an attenuated first step has been observed, a maximum 4π-periodic supercurrent contribution of $I_{4\pi} = \frac{hf_{4\pi}}{2eR_N} \leq 136$ nA (*8*) at 12 mK can be estimated for JJ-wide3. The relative amount of 4π-periodic contributions to the total supercurrent measures $I_{4\pi}/I_c = 0.34$. Next,

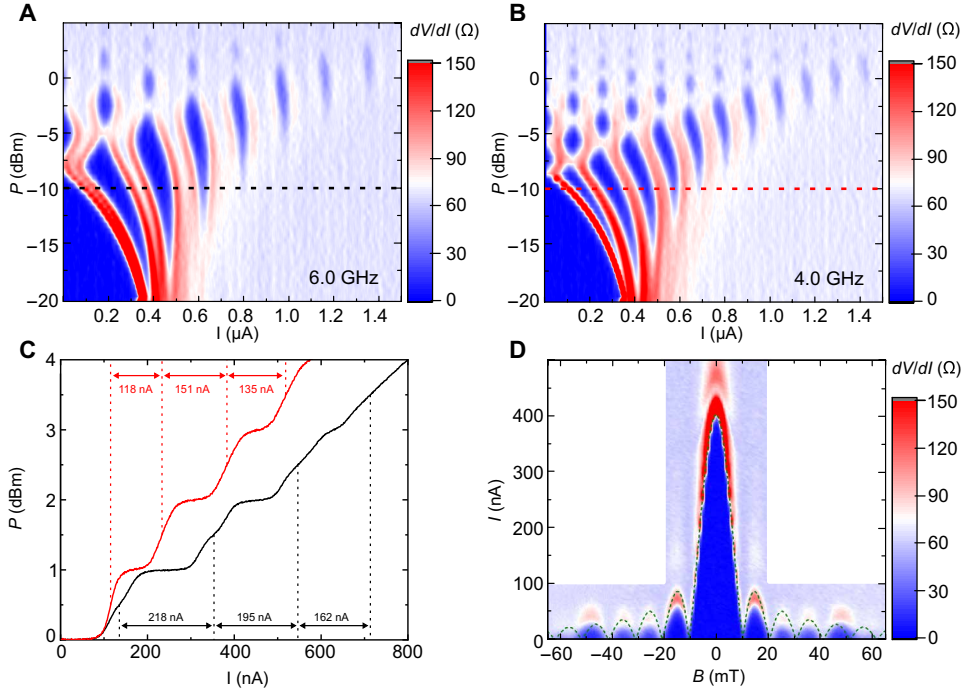

Fig. 2. Measurements on the 600-nm-wide Josephson junction JJ-wide3. (**A** and **B**) Color-coded differential resistance as a function of the applied bias current and the applied power of the rf signal $dV/dI(I, P)$ at 6.0 and 4.0 GHz, respectively. In (**C**), the Shapiro step width (in amperes) is compared for both frequencies applied at −10 dBm of the applied rf power. It can be seen that the first Shapiro step at 4.0-GHz excitation frequency (red curve) is attenuated, compared to the second step. At 6.0-GHz excitation frequency, the first step is wider than the second. (**D**) Magnetic field–dependent differential resistance $dV/dI(B)$ measured in between $-65\ \text{mT} \leq B \leq 65\ \text{mT}$. The dashed green line shows a modeled Fraunhofer pattern using an effective area model (*41*).

to the supercurrent carried by the gapless MBSs, other effects can evoke 4π-periodic supercurrent contributions. Fabry-Pérot type resonances in between the electrodes result in perfect transmission in the normal conducting state of the junction and will establish gapless bound states in the superconducting state (*16*). The normal state transmission is maximal, when a multiple of the Fermi wavelength in propagation direction fits in between the superconducting electrodes $k_xL = n\pi$. As the Fermi velocity in the BST thin film is high, $v_F = 3.8 \times 10^5$ m/s (*38*), and the distance from the Fermi energy to the Dirac point is small, $E_F - E_{DP} = 24$ meV, the Fermi wavelength $\lambda_F = 60$ nm within the BST weak link is greater than the junction length $L = 31$ nm. Hence, no resonances are expected (for more information, the reader is referred to section SA). Because of the reduced probability of normal reflections and the short junction length, however, the energy gap for modes at small angles around the perpendicular incident mode becomes small compared to thermal fluctuations ($E_{gap} < k_BT$). A broad transmission maximum around the perpendicular incident mode evokes additional 4π-periodic supercurrent contributions and explains the relative amount of $I_{4\pi}$ that has been determined (see fig. S1).

To verify the spatial dimensions of JJ-wide3, magnetic field–dependent measurements have been performed and show regular Fraunhofer pattern. The magnetic field–dependent differential resistance (dV/dI) has been measured making use of standard lock-in techniques. Results for JJ-wide3 are shown in Fig. 2D and in fig. S2 for the other junctions. The superconducting region ($dV/dI = 0$) is displayed in blue, while the resistive regime of the junction is shown in red/white. The position of the side maxima within the Fraunhofer pattern can be observed to change with the junction length (see section SB). An effective area model (*41*) has been used to fit the expected Fraunhofer pattern based on the measured data. The fit is shown as dashed dark green line in Fig. 2D and is in good agreement with the measured data. The observation of a regular Fraunhofer pattern indicates a homogeneous current distribution within the BST weak link.

We now focus on the investigation of junctions on narrow BST nanoribbons of only $W = 200$ nm that have been defined using a SAG approach (*24*, *36*, *37*). In Josephson junctions on selectively deposited nanoribbons, the geometry of the junction is defined by the width W of the TI nanoribbon and the electrode separation L of the two superconducting electrodes. The device layout is schematically shown in Fig. 3A. As an example, a 200-nm-wide, selectively grown ternary TI nanoribbon with sputter-deposited superconducting Nb electrodes is shown in Fig. 3B. For details on the substrate preparation for the SAG of 3D TI compounds using MBE, the reader is referred to Materials and Methods. A cross-sectional analysis of SAG-grown nanoribbons is presented in (*37*).

Within BST nanoribbon devices, the wave function of topological surface states extends phase-coherently around the perimeter P. Because of spin-momentum locking, a Berry phase of π is picked up by surface charges that traverse the nanoribbon perimeter (*6*). Because of this inherent Berry phase, the boundary conditions of self-interfering charges on the perimeter are anti-periodic, which necessitates a gap (displayed in Fig. 3C) within the surface state spectrum of size (*26*)

$$\Delta_c = \frac{2\pi v_F \hbar}{P} \quad (2)$$

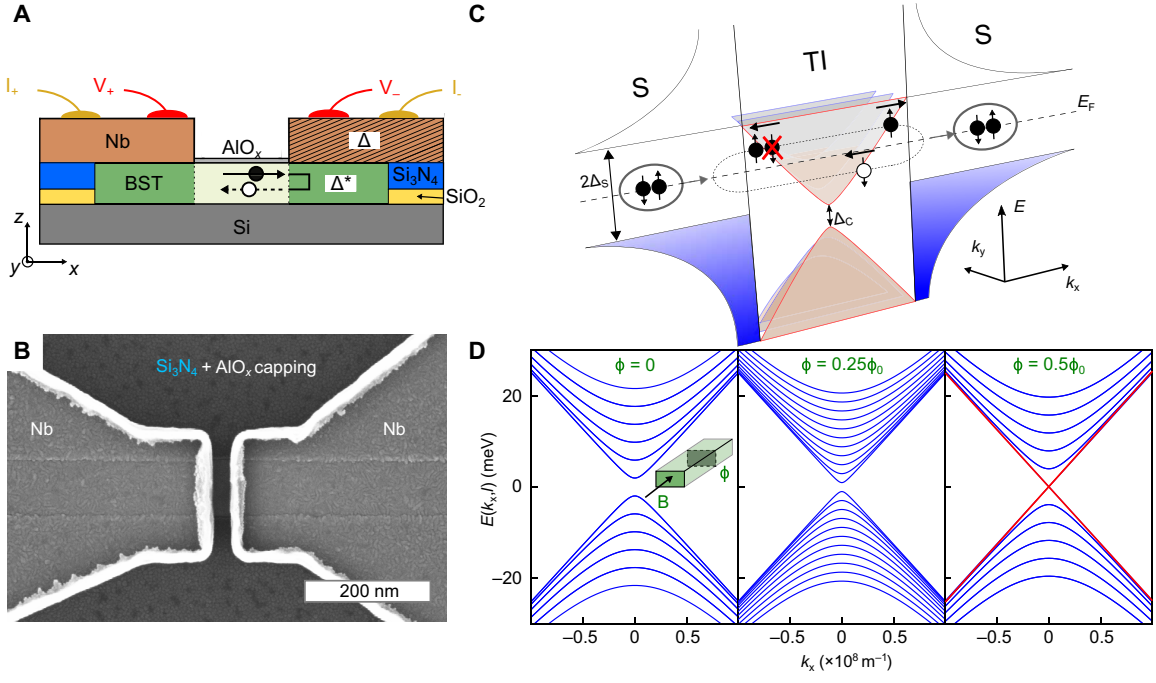

Fig. 3. Investigated Josephson junctions with quantum confinement in the BST nanoribbon weak link. (**A**) Schematic layout of the Josephson junction defined by two superconducting electrodes (yellow) on top of a selectively grown TI nanoribbon (green). (**B**) Two closely spaced Nb electrodes are sputter-deposited on top of the nanoribbon, subsequently after removal of the AlO_x capping layer in the electrode area. (**C**) Because of the confinement of topological surface charges, the transverse surface modes are quantized and the surface state spectrum is gapped Δ_c. The quantized surface sub-bands at zero applied magnetic field are spin degenerate, allowing normal reflections of electrons at the TI/S interface. (**D**) Surface state energy dispersion $E(k_x, l)$ for different values of the applied magnetic flux $\Phi = B \cdot A$, where A is the cross section of the nanoribbon. When a magnetic flux of magnitude $\Phi = \Phi_0/2 = h/2e$, a pair of spin nondegenerate linear sub-bands (red lines) emerges.

where $v_F = 3.8 \times 10^5$ m/s (*38*) is the Fermi velocity. Because of confinement, sub-bands of transverse momentum states along the nanoribbon perimeter are quantized. The coaxial- and transverse-mode–dependent energy dispersion $E(k_x, l)$ is given by

$$E(k_x, l) = \pm \hbar v_F \sqrt{k_x^2 + \left(\frac{2\pi(l + 1/2 - \Phi/\Phi_0)}{P}\right)^2} \quad (3)$$

where k_x is the coaxial wave vector along the nanoribbon. The second term within the square root expression represents the transverse wave vector k_l, where the transverse mode index $l = 0, \pm 1, \pm 2, \ldots$ and Φ/Φ_0 is the applied magnetic flux through the nanoribbon cross section, normalized to the magnetic flux quantum $\Phi_0 = h/e$. The quantized transverse momentum sub-bands are schematically depicted in Fig. 3C and quantitatively displayed in Fig. 3D for different values of the applied magnetic flux. At zero applied flux, the surface state spectrum is gapped and all states are spin degenerate. Because of the spin degeneracy of states, the perfect transmission for perpendicular modes is lifted. Only for applied fluxes of magnitude $\Phi = (l + 1/2) \cdot \Phi_0$, a pair of spin nondegenerate surface bands is established. The transition from 3D topological surface states on each individual surface of the TI and quasi-1D states confined to the perimeter of a narrow TI nanoribbon is sharp, as it is solely dependent on the relation of the phase-coherence length to the nanoribbon perimeter. In previous studies, we found that for 200-nm-wide nanoribbon devices, the topological wave function traverses the perimeter phase coherently, while for devices of width $W \geq 500$ nm, this is not observed (*37*).

In both narrow nanoribbon junctions, JJ-narrow1 and JJ-narrow2, a Josephson supercurrent has been induced successfully. The characteristic parameters of these narrow junctions are listed in Table 1. To confirm the junction (nano-)dimensions, the differential resistance dV/dI of junction JJ-narrow1 as a function of the applied perpendicular magnetic field B and the dc bias I is shown in Fig. 4A. The superconducting region ($dV/dI = 0$) is displayed in blue, while the resistive regime of the junction is shown in red/white. The differential resistance shows a full suppression of the critical current at 31.7 mT. A reappearance of the supercurrent is observed for larger magnetic field values. Modeling the data using previously mentioned effective area model did not result in a good fit to the measured data. For the BST nanoribbon–based junctions, it needs to be considered that the junction dimensions are defined by the electrode separation distance $L = 31$ nm and the width $W = 200$ nm of the TI nanoribbon (see Fig. 3B). The effective area model has been adapted to the nanoribbon geometry given by

$$A_{eff} = W \cdot L + 2 \cdot \left[a \cdot W + \frac{1}{2}\left(\frac{W}{2} + x\right)^2 + \frac{1}{2}\left(\frac{W}{2} - x\right)^2 + 2x \cdot \left(\frac{W}{2} - x\right)\right] \quad (4)$$

Here, x is the offset from the middle of the nanoribbon, with respect to the middle of the superconducting electrode along the wire axis, and a is the extent of the electrode next to the nanoribbon (see Fig. 5B). The model thereby also accounts for an asymmetry of the deposited leads with respect to the nanoribbon. The effective area determined using the adapted effective area model has been used to fit a Fraunhofer diffraction pattern to the dV/dI data in Fig. 5A using $I_c = 30$ nA. The resulting fit (green trace) is in good agreement with the measured data.

After verifying the junction dimensions, we continue to estimate the expected 4π-periodic supercurrent contributions to the total supercurrent across the BST nanoribbon weak link. The IV curve of JJ-narrow1 and the corresponding differential resistance (dV/dI) trace are displayed in Fig. 5A. The critical switching current measures $I_c = 30$ nA, and the retrapping current $I_r = 22$ nA. In Fig. 5B, the values of I_c and I_r are plotted as a function of temperature up to 700 mK. Above this temperature, no Josephson supercurrent is observed anymore. The junction is slightly hysteretic up to about 250 mK, which can be explained by self-heating mechanisms or capacitances that affect the junction dynamics (*17*, *42*). The kink in the $I_c(T)$ data at around 400 mK is due to the coexistence of diffusive and ballistic supercurrent channels in topological Josephson junctions (*17*). The $I_c(T)$ data presented here have been fitted using a diffusive model based on the Usadel equations (blue curve) and a ballistic model based on the Eilenberger equations (red curve) (*17*). The total fit as the sum of both ballistic and diffusive current contributions is shown as a black curve. The best fit performed results in a near-unity transparency ($D = 0.95$) for the ballistic channel. Different critical temperatures can be attributed to diffusive bulk ($T_{c,diff} = 0.5$) and ballistic surface contributions ($T_{c,ball} = 0.9$), respectively. At base temperature, the ratio of ballistic surface contributions to diffusive bulk contributions is $I_{c,ball}/I_{c,diff} = 0.6$. At higher temperatures, this

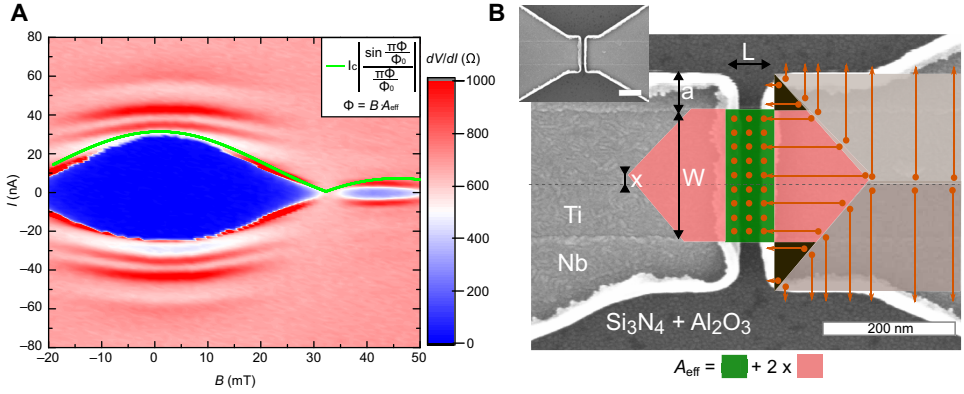

Fig. 4. Magnetic field dependency of JJ-narrow1. (**A**) Within the differential resistance (dV/dI) map, the superconducting regions are depicted in blue and the dissipative regions are depicted in white/red. The green curve fit shows the calculated Fraunhofer diffraction pattern using an effective area A_{eff} model. (**B**) Proposed model to fit the suppression of the critical current I_c in (A) based on the deflection of magnetic field lines (orange dots and arrows). The highlighted additional areas on the superconducting electrodes (pink) add to the effective area of the junction (green). The highlighted geometric lengths display the variables used in Eq. 4.

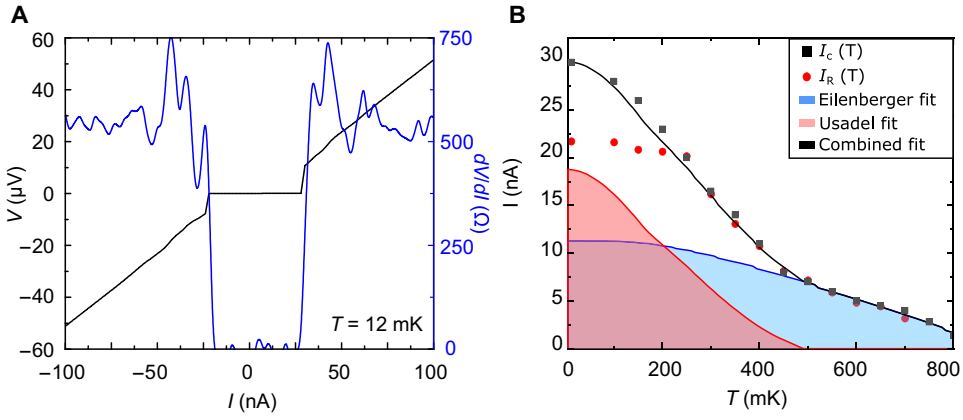

Fig. 5. *IV* characteristics of the TI nanoribbon–based Josephson junctions. (**A**) *IV* curve (black line) and *dV*/*dI* characteristics (blue curve) of JJ-narrow1 at low bias currents. (**B**) Temperature dependence of the critical switching current I_c (black squares) and the retrapping current I_r (red dots). The junction shows hysteretic behavior up to a temperature of about 250 mK. The blue line shows the ballistic Eilenberger fit, the red line shows the diffusive Usadel fit, and the black line shows the combined fit performed.

ratio increases until the critical current is solely carried by ballistic surface modes ($T \geq T_{c,diff}$). For more information on the $I_c(T)$ fitting procedure, the reader is referred to section SC.

For a relative amount of 4π-periodic supercurrent contributions as determined for the wide junction, the expected value would be $I_{4\pi} = 0.34 \times 30$ nA = 10.5 nA. On the basis of the temperature-dependent $I_c(T)$ data presented in Fig. 5B, the absolute amount of 4π-periodic supercurrent contributions should not change at 300 mK, while the relative amount is increased. The maximum crossover frequency for the observation of an attenuated first Shapiro step is therefore expected at $f_{4\pi} = \frac{2eR_N I_{4\pi}}{h} = 2.8$ GHz. Surely not all the surface modes will carry a 4π-periodic supercurrent, as only the perpendicular incident mode has perfect transmission in these short junctions ($L < \lambda_F$). We again consider 4π-periodic suppercurrent contributions from thermal excitations across the energetic gap within the bound state spectrum by modeling the size of E_{gap} around the perpendicular incident mode. Here, we include the confinement in k_l given in Eq. 3. It can be shown that at least half of the surface modes contribute to a 4π-periodic supercurrent (for further details, the reader is referred to section SA). The minimum crossover frequency for the observation of an attenuated first Shapiro step is therefore expected at $f_{4\pi} = 1.4$ GHz. To probe the periodicity of bound states developed within the induced superconducting gap inside the TI nanoribbon weak link, the Shapiro response of JJ-narrow1 has been measured within the experimental range of 4.2 GHz $\geq f \geq$ 1.6 GHz. Figure 6 (A to D) shows maps of the differential resistance *dV*/*dI* as a function of the bias potential *V* and the power level *P* of the applied rf signal. The bias potential *V* is normalized to the Shapiro step separation voltage V_0. As previously mentioned, due to the difference in superconducting coherence lengths of ballistic and diffusive modes ($\xi_{ball} > \xi_{diff}$), it is possible to increase the ratio of the ballistic to diffusive supercurrent contributions by measuring the Shapiro response at higher temperatures (*17*). Measuring at elevated temperatures $T > T_{base}$ will remove the hysteresis of the critical current I_c and retrapping current I_r. Therefore, Shapiro response measurements have been performed at 300 mK, at which the critical switching current in JJ-narrow1 has been measured to be $I_{c,300\,mK} = 17$ nA. For these applied rfs, all integer Shapiro steps have been identified. That indications of gapless bound states are absent in the rf response of these narrow nanoribbon junctions can only be explained by the absence of the perfectly transmitted mode at perpendicular incidence. This is an indication of the quantization of transverse momentum sub-bands on the nanoribbon surface and the affiliated spin degeneracy of these surface states.

DISCUSSION

Ex situ defined Josephson devices of $W = 600$ nm have been defined on AlO_x capped BST thin films. Narrow, 200-nm-wide junctions on selectively grown TI nanoribbons have been defined using a SAG approach. *IV* characteristics, magnetic field–dependent critical current modulations, and the Shapiro response upon application of an rf signal have been determined for both sets of junctions.

Upon the application of a perpendicular magnetic field, it has been possible to suppress the Josephson supercurrent in all junctions being investigated. An effective area model has been used to verify the junction dimensions (*41*), which has been further adapted to verify the spatial extent of the nanoribbon-based junctions within the scope of this work.

Compared to previously reported in situ defined junctions (*17*), the critical current values and I_cR_N products of investigated junctions here are smaller. The junction current voltage characteristics, however, show fully developed induced superconducting gaps, and the characteristic values are consistent within themselves. The I_cR_N values determined show that the size of the proximity induced gap is about the same in all junctions.

The total Josephson supercurrent has been identified to be carried by both diffusive bulk and ballistic surface contributions. While the in situ capping of devices is of crucial importance, the interfacial transparency in between the BST nanoribbon and the Nb electrodes does not need to be perfect to properly proximitize the BST surface states. The size of the induced gap, however, is strongly influenced by this transparency and so is the total amount of the Josephson supercurrent.

The response of the junctions to an externally applied rf signal has been measured at different applied frequencies to identify the bound states CΦR. Differential resistance maps as a function of the junction bias and the rf power level have been measured. In the range

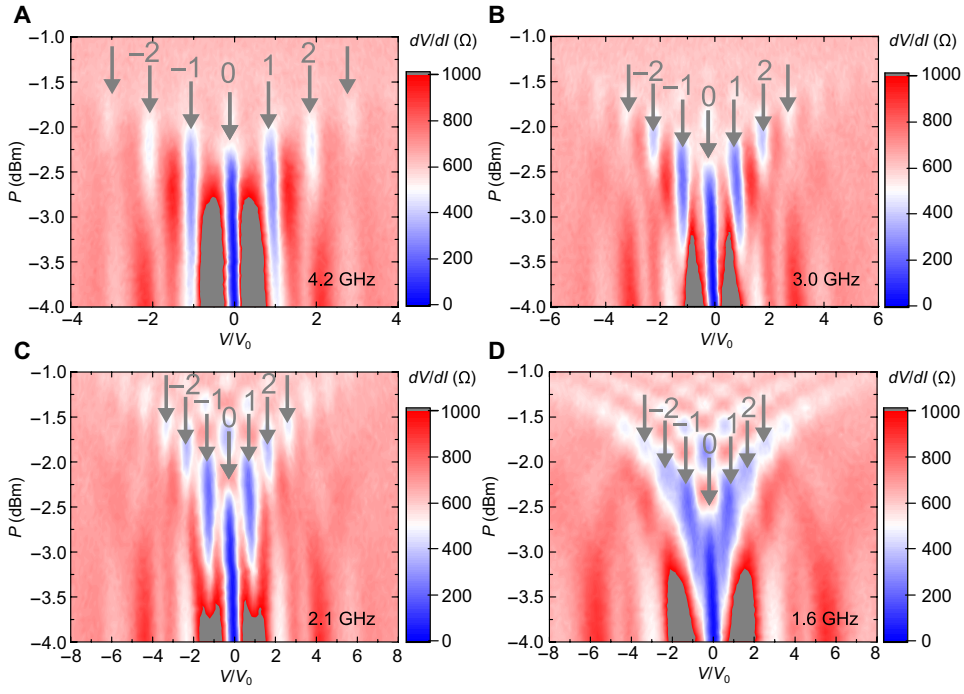

Fig. 6. Differential resistance (*dV/dI*) of JJ-narrow1 measured as a function of the applied rf power level *P* and the junction voltage bias *V* normalized to the Shapiro step separation voltage $V_0 = hf/2e$. The differential resistance maps have been measured at (**A**) 4.2 GHz, (**B**) 3.0 GHz, (**C**) 2.1 GHz, and (**D**) 1.6 GHz. Shapiro steps occur as zero differential resistance regions in dark blue. Measurements are taken at a temperature of 300 mK.

of experimentally applied rf signals, the 600- and 200-nm-wide junctions show clear distinctions.

For the 600-nm-wide junctions, an attenuated first Shapiro step has been identified, indicating the presence of 4π-periodic, gapless bound states within the BST ternary compound weak link arising from the spin texture within the TI surface states. This observation is in line with a previously reported missing first step in in situ defined Josephson junctions within junctions of higher I_c values. Although the interface of these ex situ defined junctions in between Nb and TI is not as transparent as for previously reported in situ (*17*) junctions, it is still possible to observe these signatures of 4π-periodic supercurrent contributions.

For the 200-nm-wide nanoribbon Josephson junctions, a conventional Shapiro response of Shapiro step separation width V_0 without attenuated first step has been identified. Results indicate that only conventional ABSs develop within these narrow junctions. Because of the small cross section of the TI nanoribbon weak link and the confinement of surface charges to the nanoribbon perimeter *P*, transverse momentum states within the TI nanoribbon geometry are quantized (*25*, *27*). Without any applied flux through the nanoribbon cross section, these quantized surface states are gapped and spin degenerate. The spin degeneracy enhances backscattering probabilities and prevents the formation of MBSs, which leads to the observation of conventional, full integer Shapiro steps (*26*).

In the scope of this work, it has been shown that MBSs in topological Josephson junctions can be identified without making use of complex fabrication techniques to increase the transparency at the TI/SC interface. The size of the induced gap within the BST compound underneath the superconducting electrodes seems to be decreased compared to in situ junctions, but the junction behavior is preserved using the dielectric capping layer. These observations could drive future experiments on uncharacterized topological materials to identify possible 4π-periodic CΦRs and MBS contributions. Within the same experimental range, signatures of MBSs have been absent in TI nanoribbon–based Josephson junctions, possibly due to the quantization of transverse momentum states. Conventional 2π-periodic ABSs observed here are first indications for a quasi-1D confinement within TI nanoribbon weak link Josephson junctions. A magnetic flux of $\Phi = \Phi_0/2$ piercing the nanoribbon cross section should lead to a topological phase transition. Experiments in a parallel applied magnetic field should be performed to further evaluate our findings.

MATERIALS AND METHODS

Selective area growth

To create a patterned substrate for the SAG, first, a 5-nm-thin SiO_2 layer was created by thermally oxidizing the Si(111) surface. Thereafter, a 20-nm-thick Si_3N_4 layer was deposited globally using a low-pressure chemical vapor deposition process. The SiO_2 buffer layer was used to remove any strain Si_3N_4 imposed onto the Si(111) surface. Nanotrenches, for definition of the TI nanoribbons, were defined by wet- and dry-chemical etching using the AR-P 6200 positive electron beam resist. Therefore, a reactive ion etching process with a CHF_3 and O_2 gas mixture was performed. After resist removal, the SiO_2 within the nanotrenches was wet chemically removed using hydrofluoric acid.

The BST ternary TI grew in the Te overpressure regime at T_{sub} = 290°C selectively within the defined nanotrenches. After TI deposition, a 2- to 3-nm-thin Al layer was deposited globally by MBE, which fully oxidized ex situ. The resulting AlO_x dielectric capping layer was used to protect the TI film from oxidation or from any other kind of reconstruction due to chemically reacting with air.

Superconducting contact deposition

Nb superconducting electrodes were deposited ex situ using dc magnetron sputtering. A three-layer poly(methyl methacrylate)–positive electron beam lithography resist process was used to define the electrodes with sub–100-nm separation for the definition of lateral Josephson junctions. Before the Nb deposition, the AlO_x capping layer was removed using the alkaline Fujifilm OPD 4262 3.8% tetramethylammonium hydroxide-based developer. Inside the dc magnetron sputter tool, a soft 30-s Ar etch at 6 W was used to remove oxide residuals just before the deposition of Nb.

Measurement setup

Rf and dc, low-temperature transport measurements were performed in a dilution refrigerator at a base temperature of 12 mK. The dilution refrigerator is equipped with a superconducting magnet that can apply a magnetic field up to 6 T perpendicular, out of plane, to the Josephson junctions. The Josephson junctions were characterized using a standard quasi–four-terminal setup. The differential resistance (dV/dI) was determined using standard lock-in techniques. The rf was applied to the devices using an rf generator, a stainless steel coaxial cable with a standard SubMiniature version A adapter, and a $\lambda/4$ antenna within the cylindrical sample volume.

SUPPLEMENTARY MATERIALS

Supplementary material for this article is available at http://advances.sciencemag.org/cgi/content/full/7/26/eabf1854/DC1

REFERENCES AND NOTES

1. T. Hyart, B. van Heck, I. C. Fulga, M. Burrello, A. R. Akhmerov, C. W. J. Beenakker, Flux-controlled quantum computation with Majorana fermions. *Phys. Rev. B* **88**, 035121 (2013).
2. T. Karzig, C. Knapp, R. M. Lutchyn, P. Bonderson, M. B. Hastings, C. Nayak, J. Alicea, K. Flensberg, S. Plugge, Y. Oreg, C. M. Marcus, M. H. Freedman, Scalable designs for quasiparticle-poisoning-protected topological quantum computation with Majorana zero modes. *Phys. Rev. B* **95**, 235305 (2017).
3. J. Manousakis, A. Altland, D. Bagrets, R. Egger, Y. Ando, Majorana qubits in a topological insulator nanoribbon architecture. *Phys. Rev. B* **95**, 165424 (2017).
4. L. Fu, C. L. Kane, Superconducting proximity effect and majorana fermions at the surface of a topological insulator. *Phys. Rev. Lett.* **100**, 096407 (2008).
5. A. Cook, M. Franz, Majorana fermions in a topological-insulator nanowire proximity-coupled to an *s*-wave superconductor. *Phys. Rev. B* **84**, 201105 (2011).
6. L. Fu, C. L. Kane, E. J. Mele, Topological insulators in three dimensions. *Phys. Rev. Lett.* **98**, 106803 (2007).
7. L. Fu, C. L. Kane, Josephson current and noise at a superconductor/ quantum-spin-Hall-insulator/ superconductor junction. *Phys. Rev. B* **79**, 161408 (2009).
8. J. Wiedenmann, E. Bocquillon, R. S. Deacon, S. Hartinger, O. Herrmann, T. M. Klapwijk, L. Maier, C. Ames, C. Brüne, C. Gould, A. Oiwa, K. Ishibashi, S. Tarucha, H. Buhmann, L. W. Molenkamp, 4π-periodic Josephson supercurrent in HgTe-based topological Josephson junctions. *Nat. Commun.* **7**, 10303 (2015).
9. F. Dominguez, F. Hassler, G. Platero, Dynamical detection of Majorana fermions in current-biased nanowires. *Phys. Rev. B* **86**, 140503 (2012).
10. F. Dominguez, O. Kashuba, E. Bocquillon, J. Wiedenmann, R. S. Deacon, T. M. Klapwijk, G. Platero, L. W. Molenkamp, B. Trauzettel, E. M. Hankiewicz, Josephson junction dynamics in the presence of 2π- and 4π-periodic supercurrents. *Phys. Rev. B* **95**, 195430 (2017).
11. L. P. Rokhinson, X. Liu, J. K. Furdyna, The fractional a.c. Josephson effect in a semiconductor–superconductor nanowire as a signature of Majorana particles. *Nat. Phys.* **8**, 795–799 (2012).
12. M. C. Dartiailh, W. Mayer, J. Yuan, K. S. Wickramasinghe, A. Matos-Abiague, I. Zutić, J. Shabani, Phase signature of topological transition in josephson junctions. *Phys. Rev. Lett.* **126**, 036802 (2021).
13. H. Ren, F. Pientka, S. Hart, A. T. Pierce, M. Kosowsky, L. Lunczer, R. Schlereth, B. Scharf, E. M. Hankiewicz, L. W. Molenkamp, B. I. Halperin, A. Yacoby, Topological superconductivity in a phase-controlled Josephson junction. *Nature* **569**, 93–98 (2019).
14. S. Shapiro, Josephson currents in superconducting tunneling: The effect of microwaves and other observations. *Phys. Rev. Lett.* **11**, 80–82 (1963).
15. E. Bocquillon, R. S. Deacon, J. Wiedenmann, P. Leubner, T. M. Klapwijk, C. Brüne, K. Ishibashi, H. Buhmann, L. W. Molenkamp, Gapless Andreev bound states in the quantum spin Hall insulator HgTe. *Nat. Nanotechnol.* **12**, 137–143 (2016).
16. C. Li, J. C. de Boer, B. de Ronde, S. V. Ramankutty, E. van Heumen, Y. Huang, A. de Visser, A. A. Golubov, M. Golden, A. Brinkman, 4π-periodic Andreev bound states in a Dirac semimetal. *Nat. Mater.* **17**, 875–880 (2018).
17. P. Schüffelgen, D. Rosenbach, C. Li, T. W. Schmitt, M. Schleenvoigt, A. R. Jalil, S. Schmitt, J. Kölzer, M. Wang, B. Bennemann, U. Parlak, L. Kibkalo, S. Trellenkamp, T. Grap, D. Meertens, M. Luysberg, G. Mussler, E. Berenschot, N. Tas, A. A. Golubov, A. Brinkman, T. Schäpers, D. Grützmacher, Selective area growth and stencil lithography for in situ fabricated quantum devices. *Nat. Nanotechnol.* **14**, 825–831 (2019).
18. K. Le Calvez, L. Veyrat, F. Gay, P. Plaindoux, C. B. Winkelmann, H. Courtois, B. Sacépé, Joule overheating poisons the fractional ac Josephson effect in topological Josephson junctions. *Commun. Phys.* **2**, 4 (2019).
19. S. A. Khan, C. Lampadaris, A. Cui, L. Stampfer, Y. Liu, S. J. Pauka, M. E. Cachaza, E. M. Fiordaliso, J.-H. Kang, S. Korneychuk, T. Mutas, J. E. Sestoft, F. Krizek, R. Tanta, M. C. Cassidy, T. S. Jespersen, P. Krogstrup, Highly transparent gatable superconducting shadow junctions. *ACS Nano* **14**, 14605–14615 (2020).
20. M. Lang, L. He, F. Xiu, X. Yu, J. Tang, Y. Wang, X. Kou, W. Jiang, A. V. Fedorov, K. L. Wang, Revelation of topological surface states in Bi_2Se_3 thin films by in situ Al passivation. *ACS Nano* **6**, 295–302 (2011).
21. P. Ngabonziza, R. Heimbuch, N. de Jong, R. A. Klaassen, M. P. Stehno, M. Snelder, A. Solmaz, S. V. Ramankutty, E. Frantzeskakis, E. van Heumen, G. Koster, M. S. Golden, H. J. W. Zandvliet, A. Brinkman, In situ spectroscopy of intrinsic Bi_2Te_3 topological insulator thin films and impact of extrinsic defects. *Phys. Rev. B* **92**, 035405 (2015).
22. Y. Takeshige, S. Matsuo, R. S. Deacon, K. Ueda, Y. Sato, Y.-F. Zhao, L. Zhou, C.-Z. Chang, K. Ishibashi, S. Tarucha, Experimental study of ac Josephson effect in gate-tunable $(Bi_{1-x}Sb_x)_2Te_3$ thin-film Josephson junctions. *Phys. Rev. B* **101**, 115410 (2020).
23. C. Weyrich, M. Lanius, P. Schüffelgen, D. Rosenbach, G. Mussler, S. Bunte, S. Trellenkamp, D. Grützmacher, T. Schäpers, Phase-coherent transport in selectively grown topological insulator nanodots. *Nanotechnology* **30**, 055201 (2018).
24. K. Moors, P. Schüffelgen, D. Rosenbach, T. W. Schmitt, T. Schäpers, T. L. Schmidt, Magnetotransport signatures of three-dimensional topological insulator nanostructures. *Phys. Rev. B* **97**, 245429 (2018).
25. Y. Zhang, Y. Ran, A. Vishwanath, Topological insulators in three dimensions from spontaneous symmetry breaking. *Phys. Rev. B* **79**, 245331 (2009).
26. J. H. Bardarson, P. W. Brouwer, J. E. Moore, Aharonov-Bohm oscillations in disordered topological insulator nanowires. *Phys. Rev. Lett.* **105**, 156803 (2010).
27. A. M. Cook, M. M. Vazifeh, M. Franz, Stability of Majorana fermions in proximity-coupled topological insulator nanowires. *Phys. Rev. B* **86**, 155431 (2012).
28. J. H. Bardarson, J. E. Moore, Quantum interference and Aharonov-Bohm oscillations in topological insulators. *Rep. Prog. Phys.* **76**, 056501 (2013).
29. D. Laroche, D. Bouman, D. J. van Woerkom, A. Proutski, C. Murthy, D. I. Pikulin, C. Nayak, R. J. J. van Gulik, J. Nygård, P. Krogstrup, L. P. Kouwenhoven, A. Geresdi, Observation of the 4π-periodic Josephson effect in indium arsenide nanowires. *Nat. Commun.* **10**, 245 (2019).
30. H. Peng, K. Lai, D. Kong, S. Meister, Y. Chen, X.-L. Qi, S.-C. Zhang, Z.-X. Shen, Y. Cui, Aharonov-Bohm interference in topological insulator nanoribbons. *Nat. Mater.* **9**, 225–229 (2010).
31. Y. Zhang, A. Vishwanath, Anomalous Aharonov-Bohm conductance oscillations from topological insulator surface states. *Phys. Rev. Lett.* **105**, 206601 (2010).
32. F. Xiu, L. He, Y. Wang, L. Cheng, L.-T. Chang, M. Lang, G. Huang, X. Kou, Y. Zhou, X. Jiang, Z. Chen, J. Zou, A. Shailos, K. L. Wang, Manipulating surface states in topological insulator nanoribbons. *Nat. Nanotechnol.* **6**, 216–221 (2011).
33. S. Cho, B. Dellabetta, R. Zhong, J. Schneeloch, T. Liu, G. Gu, M. J. Gilbert, N. Mason, Aharonov-Bohm oscillations in a quasi-ballistic three-dimensional topological insulator nanowire. *Nat. Commun.* **6**, 7634 (2015).
34. L. A. Jauregui, M. T. Pettes, L. P. Rokhinson, L. Shi, Y. P. Chen, Magnetic field-induced helical mode and topological transitions in a topological insulator nanoribbon. *Nat. Nanotechnol.* **11**, 345–351 (2016).
35. Y. C. Arango, L. Huang, C. Chen, J. Avila, M. C. Asensio, D. Grützmacher, H. Lüth, J. G. Lu, T. Schäpers, Quantum transport and nano angle-resolved photoemission spectroscopy on the topological surface states of single Sb_2Te_3 nanowires. *Sci. Rep.* **6**, 29493 (2016).
36. J. Kölzer, D. Rosenbach, C. Weyrich, T. W. Schmitt, M. Schleenvoigt, A. R. Jalil, P. Schüffelgen, G. Mussler, V. E. Sacksteder, D. Grützmacher, H. Lüth, T. Schäpers, Phase-coherent loops in selectively-grown topological insulator nanoribbons. *Nanotechnology* **31**, 325001 (2020).
37. D. Rosenbach, N. Oellers, A. R. Jalil, M. Mikulics, J. Kölzer, E. Zimmermann, G. Mussler, S. Bunte, D. Grützmacher, H. Lüth, T. Schäpers, Quantum transport in topological surface states of Bi_2Te_3 nanoribbons. *Adv. Electron. Mater.* **6**, 2000205 (2020).
38. J. Kellner, M. Eschbach, J. Kampmeier, M. Lanius, E. Mlynczak, G. Mussler, B. Holländer, L. Plucinski, M. Liebmann, D. Grützmacher, C. M. Schneider, M. Morgenstern, Tuning

the Dirac point to the Fermi level in the ternary topological insulator $(Bi_{1-x}Sb_x)_2Te_3$. *Appl. Phys. Lett.* **107**, 251603 (2015).
39. P. Roushan, J. Seo, C. V. Parker, Y. S. Hor, D. Hsieh, D. Qian, A. Richardella, M. Z. Hasan, R. J. Cava, A. Yazdani, Topological surface states protected from backscattering by chiral spin texture. *Nature* **460**, 1106–1109 (2009).
40. M. Snelder, M. Veldhorst, A. A. Golubov, A. Brinkman, Andreev bound states and current-phase relations in three-dimensional topological insulators. *Phys. Rev. B* **87**, 104507 (2013).
41. C. Molenaar, D. Leusink, X. Wang, A. Brinkman, Geometric dependence of Nb-Bi_2Te_3-Nb topological Josephson junction transport parameters. *Supercond. Sci. Technol.* **27**, 104003 (2014).
42. H. Courtois, M. Meschke, J. T. Peltonen, J. P. Pekola, Origin of hysteresis in a proximity josephson junction. *Phys. Rev. Lett.* **101**, 067002 (2008).
43. C. W. J. Beenakker, H. van Houten, Josephson current through a superconducting quantum point contact shorter than the coherence length. *Phys. Rev. Lett.* **66**, 3056–3059 (1991).
44. K. D. Usadel, Generalized diffusion equation for superconducting alloys. *Phys. Rev. Lett.* **25**, 507–509 (1970).
45. J. Dufouleur, L. Veyrat, B. Dassonneville, C. Nowka, S. Hampel, P. Leksin, B. Eichler, O. G. Schmidt, B. Büchner, R. Giraud, Enhanced mobility of spin-helical Dirac fermions in disordered 3D topological insulators. *Nano Lett.* **16**, 6733–6737 (2016).
46. A. V. Galaktionov, A. D. Zaikin, Quantum interference and supercurrent in multiple-barrier proximity structures. *Phys. Rev. B* **65**, 184507 (2002).
47. A. Brinkman, A. A. Golubov, Coherence effects in double-barrier Josephson junctions. *Phys. Rev. B* **61**, 11297–11300 (2000).
48. M. Y. Kupriyanov, V. F. Lukichev, Influence of boundary transparency on the critical current of "dirty" SS'S structures. *Zh. Eksp. Teor. Fiz.* **94**, 139–149 (1988).

Acknowledgments: We thank D. Veldhuis for the etching of the AlO_x capping layer and the deposition of the Nb electrodes. We also thank G. P. Nagda for proofreading the manuscript. **Funding:** This work was financially supported by the Virtual Institute for Topological Insulators (VITI), which is funded by the Helmholtz Association (VH-VI-511). This work was financially supported by the Netherlands Organization for Scientific Research (NWO) through a VENI grant (680-47-463). This work was financially supported by the German Federal Ministry of Education and Research (BMBF) via the Quantum Futur project "MajoranaChips" (Grant No. 13N15264) within the funding program Photonic Research Germany. This work was partly funded by the Deutsche Forschungsgemeinschaft (DFG, German Research Foundation) under Germany's Excellence Strategy—Cluster of Excellence Matter and Light for Quantum Computing (ML4Q) EXC 2004/1—390534769. **Author contributions:** D.R. and T.W.S. fabricated the substrates in the cleanroom. S.T. performed electron beam lithography. P.S., M.S., A.R.J., and G.M. grew the topological insulator thin films and nanoribbons via MBE and capped the samples in situ. D.R., T.W.S., P.S., M.P.S., and C.L. performed the electrical transport measurements on Josephson devices. T.W.S. and E.N. performed the focused ion beam investigations on the TI nanoribbon cross section. D.R. carried out the Eilenberger and Usadel fitting with the supervision of A.A.G. and A.B. The paper has been written by D.R. with contributions from all coauthors. The project was supervised by A.A.G., A.B., D.G., and T.S. **Competing interests:** The authors declare that they have no competing interests. **Data and materials availability:** All data needed to evaluate the conclusions in the paper are present in the paper and/or the Supplementary Materials. The source data underlying Figs. 2 and 4 to 6 and figs. S1 and S2 are provided as a source data file from the Jülich DATA repository (https://doi.org/10.26165/JUELICH-DATA/A6DGGW).

Submitted 9 October 2020
Accepted 12 May 2021
Published 23 June 2021
10.1126/sciadv.abf1854

Citation: D. Rosenbach, T. W. Schmitt, P. Schüffelgen, M. P. Stehno, C. Li, M. Schleenvoigt, A. R. Jalil, G. Mussler, E. Neumann, S. Trellenkamp, A. A. Golubov, A. Brinkman, D. Grützmacher, T. Schäpers, Reappearance of first Shapiro step in narrow topological Josephson junctions. *Sci. Adv.* **7**, eabf1854 (2021).